

Chiral sensing with achiral anisotropic metasurfaces

Sotiris Droulias^{1,2,*} and Lykourgos Bougas^{3,†}

¹*Institute of Electronic Structure and Laser, FORTH, 71110 Heraklion, Crete, Greece*

²*Department of Materials Science and Technology, University of Crete, 70013 Heraklion, Greece*

³*Institut für Physik, Johannes Gutenberg Universität-Mainz, 55128 Mainz, Germany*



(Received 22 February 2021; accepted 23 July 2021; published 9 August 2021)

We present a theoretical analysis for chiral sensing using achiral anisotropic metasurfaces. We derive analytically, and verify numerically, simple formulas that provide insight into the sensing mechanism and explain how anisotropic metasurfaces offer additional degrees of freedom with respect to their isotropic counterparts. We demonstrate how to deconvolve the unknown chirality from the background dispersion of the metasurface, and we propose practical measurement schemes for its unambiguous determination. Last, we discuss the key functionalities and benefits of anisotropic metasurfaces, and we provide the design principles towards broadband operation—from near-infrared to near-ultraviolet frequencies—opening the way for highly sensitive nanoscale chiroptical spectroscopy. Our numerical examples are focused on a metasurface design that we recently proposed, which belongs to the wider class of achiral anisotropic metasurfaces.

DOI: [10.1103/PhysRevB.104.075412](https://doi.org/10.1103/PhysRevB.104.075412)

I. INTRODUCTION

Chirality—a geometric property in which an object is nonsuperimposable with its mirror image—is an essential condition for the structural and functional diversity of biomolecules and many chemical compounds, which can exist in right- and left-handed forms known as enantiomers. Their functionality is often determined by their handedness, and hence the ability to efficiently sense molecular chirality is of fundamental importance for many research disciplines and industries, such as chemical, agricultural, and pharmaceutical [1,2].

A homogeneous natural optically active medium, e.g., a thin film consisting of chiral molecules, is described electromagnetically by the constitutive relations $\mathbf{D} = \epsilon_0 \epsilon \mathbf{E} - i(\kappa/c)\mathbf{H}$, $\mathbf{B} = \mu_0 \mu \mathbf{H} + i(\kappa/c)\mathbf{E}$ [3], where ϵ , μ are the relative permittivity and permeability (ϵ_0 , μ_0 are the vacuum permittivity and permeability) and c is the vacuum speed of light; κ is the chirality (also known as “Pasteur” [4]) parameter, which expresses the chiral molecular response and is, in general, complex: its magnitude, $|\kappa|$, is proportional to the sample’s density (or its concentration in a solution), and its sign, $\text{sgn}(\kappa)$, depends on the handedness of the medium [3]. Therefore, in order to be able to detect and distinguish enantiomers, a chiral sensing scheme should be sensitive to $|\kappa|$ and $\text{sgn}(\kappa)$, respectively.

Among the most widely used techniques for chiral sensing are the polarimetric techniques of optical rotatory dispersion (ORD) and circular dichroism (CD) [1], both routinely applied in industrial applications [2]. Unfortunately, and despite their extensive use, the sensitivity limits of commercially avail-

able optical spectropolarimeters are at ~ 0.1 -1-mdeg levels [5], which constrains their applicability for measurements of dilute samples (e.g., gas samples), and, particularly, of nanometer-scale thin films, where the chiroptical signals are typically $< 100 \mu\text{deg}$ (e.g., protein monolayers).

On the other hand, nanophotonic approaches for chiral sensing have allowed for the measurement of chiroptical signals unattainable using traditional polarimetric techniques. Their principle of operation is based on the excitation of superchiral near fields, that is, fields with optical chirality density [6] higher than that of circularly polarized light, and this approach is met in various schemes, such as propagating surface plasmons [7,8], plasmonic particles [9–12], chiral metamaterials [13–16], and, recently, achiral metamaterials [17–19] (we refer the reader to the reviews in Refs. [20–24] and references therein for a more detailed description of recent developments). However, almost all recent nanophotonic approaches for chiral sensing have focused their efforts on performing and enhancing CD measurements, i.e., measurements of only the imaginary part of the chirality parameter, $\text{Im}(\kappa)$. In contrast, the ability to detect $\text{Re}(\kappa)$ can be particularly useful in cases where $\text{Im}(\kappa)$ is weak, e.g., at frequencies far from the chiral molecular resonances. In addition, in most demonstrations and proposals, the employed nanophotonic systems have their own intrinsic chiroptical responses that contribute to the total measured CD signal (e.g., Refs. [14,15,25]), thus requiring separate measurements with and without the chiral inclusions to identify the chiroptical signal from the molecular system [25].

To overcome these limitations, recently, we proposed a metasurface design [26] that (i) results in enhanced chiroptical signals by more than two orders of magnitude for ultrathin, subwavelength, chiral samples over a uniform and accessible area, (ii) allows for complete measurements of the total chirality (magnitude and sign of both its real and imaginary

*sdroulias@iesl.forth.gr

†lybougas@uni-mainz.de

part), and (iii) offers the possibility for a crucial signal reversal (excitation with reversed polarization) that enables chirality measurements in an absolute manner, i.e., without the need for sample removal. The key element that enables the above functionalities is the use of the anisotropy of the metasurface, rather than the superchirality of the near fields. Our proposed design belongs to the wider class of anisotropic metasurfaces, and therefore particularly in the context of possible future experiments and applications, it is necessary to provide further insight into the underlying mechanism of chiral sensing with achiral anisotropic metasurfaces.

In this paper we extend the analytical methods introduced in Ref. [27], for the case of isotropic metasurfaces, to the development of a theoretical framework required to analyze the enhanced chiroptical signals attainable using achiral anisotropic metasurfaces. We focus on our recently proposed design [26] to discuss essential experimental aspects and design criteria for enhanced chiral sensing using, in general, achiral anisotropic metasurfaces. In particular, we provide a theoretical model for the description of achiral anisotropic metasurfaces with chiral inclusions (i.e., a chiral film) that elucidates how aspects of chiral sensing are associated with the properties of the metasurfaces. Additionally, we show that these classes of metasurfaces have the ability to differentiate the real and imaginary parts of κ , $\text{Re}(\kappa)$ and $\text{Im}(\kappa)$, respectively, in contrast to most current approaches that are focused on enhancing CD signals and, as such, are expected to be sensitive to $\text{Im}(\kappa)$ [7,13,17,18,23,25,28–32]. We derive simple analytical formulas that provide insight into the mechanism associated with different excitation conditions (linearly vs elliptically polarized waves) and explain how anisotropic metasurfaces can circumvent the trade-off met in isotropic metasurfaces, in which the far-field chiroptical response changes inversely with the transmitted power. Last, we demonstrate how to deconvolve the unknown chirality from the background dispersion of the metasurface, and we propose practical measurement schemes for the unambiguous determination of an unknown chirality, a crucial aspect in the design of future experiments, and provide the design principles towards chiroptical spectroscopy over different (broadband) spectral ranges.

II. PRINCIPLE OF OPERATION

Based on the fact that chiral matter-wave interactions require a nonvanishing pseudoscalar product between \mathbf{E} and \mathbf{B} , chirality sensing with nanophotonic systems is largely based on using two orthogonal modes of the nanophotonic system that have parallel electric and magnetic components and are also at the same frequency (we refer to the two modes as *electric* and *magnetic*) [18,33,34]. The combined action of the two modes mediates the strong near-field coupling between the nanophotonic system and the chiral inclusion, which enables enhanced far-field signals from otherwise weak chirality values κ . Although the use of two such modes is met in several other approaches (e.g., Refs. [7,14–24,33]), the key difference here is that our approach for enhanced chiral sensing is based on the anisotropic response of the metasurface, rather than the superchirality of the generated near fields; here, the electric mode and the magnetic mode are coupled via the chirality,

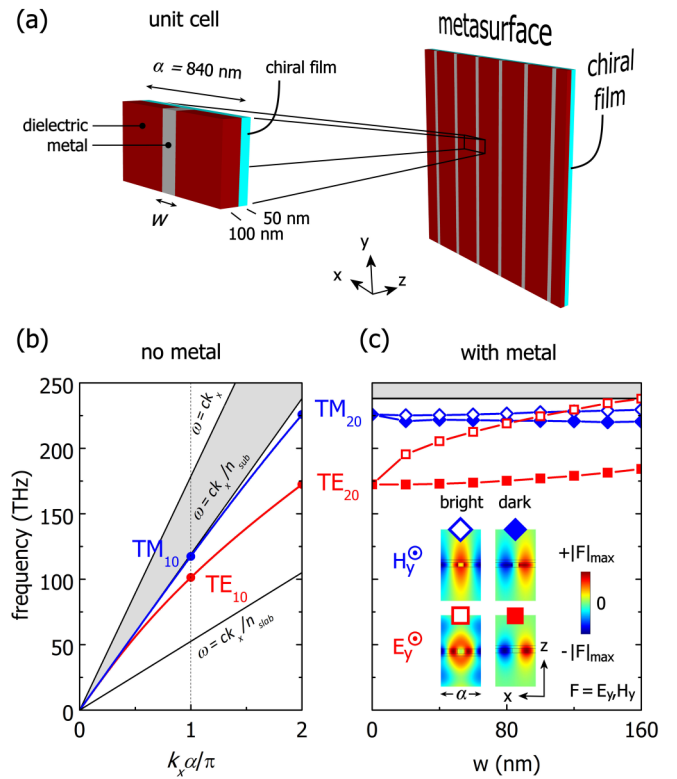


FIG. 1. Anisotropic metasurface for enhanced chiral sensing. (a) Single unit cell and schematic of the metasurface containing six unit cells. (b) Dispersion of TE_0 and TM_0 modes in the absence of metal ($\alpha = 840$ nm, $n_{\text{slab}} = 3.4$, and $n_{\text{sub}} = 1.5$). (c) Splitting of TE_{20} and TM_{20} modes and tuning of their eigenfrequencies with a periodically introduced metal of width w . Inset: Field distribution of the electric-type (TE_{20}) and magnetic-type (TM_{20}) modes for $w = 140$ nm. The modes used in this paper, i.e., the bright modes, are marked with open symbols.

and anisotropy is used to further enhance the interaction [26]. This technique has not yet been experimentally adopted, and, particularly in view of possible future experiments and applications, it is necessary to provide further insight into the underlying sensing mechanism.

Here, we focus on design parameters for chiral sensing in the near infrared, in particular, 1300 nm (~ 230 THz), and to implement the electric and the magnetic mode, we start with a 100-nm-thick dielectric slab with refractive index $n = 3.4$ (e.g., Si) [see Fig. 1(a)]. The thin slab supports TE and TM modes with continuous dispersion (see, for instance, Ref. [35]) that have components (H_x, E_y, H_z) and (E_x, H_y, E_z) , respectively; therefore we can utilize their dominant (parallel) field components, E_y and H_y , respectively. For simplicity we work with the dispersion branches corresponding to TE_0 and TM_0 , the lowest-order modes [Fig. 1(b)], although any other branch can be utilized [see Supplemental Material (SM) [36]]. Next we introduce metallic wires of the same thickness (100 nm) and width w that are infinite along the y axis, with periodicity $\alpha = 840$ nm [see Fig. 1(a)]; the metal is a Drude gold (Au) of permittivity based on Johnson and Christy data [37]. The purpose of the metallic wires is (i) to spatially quantize the continuous TE and TM slab waveguide modes

and provide discrete sets of resonant states and (ii) to perturb the symmetry of the fields across each unit cell, essentially leading to residual moments in the dominant field components of each mode, i.e., electric (magnetic) dipole moment in the E_y (H_y) component of the TE (TM) mode. Additionally, the dispersion of the composite metal-dielectric system becomes a quantized version of that of the dielectric slab, with periodicity $\pi = \alpha$. Because E_y and H_y belong to different modes, to maximize their interaction with the chiral system, we use the width, w , of the metallic wires to tune the spectral separation between the two modes, which we label TE_{20} and TM_{20} as we use the lowest-order TE_0 and TM_0 branches and we operate with the second quantized mode, i.e., at the Brillouin zone edge with $k_x\alpha/\pi = 2$ (k_x is the in-plane wave number) [Fig. 1(b)]. Note that, due to the metal, each mode splits into two versions, one having antinodes [Fig. 1(c) inset, open symbols] and the other having nodes [Fig. 1(c) inset, solid symbols] at the metal region. Among the four discretized versions, those modes with nodes at the metal region have no residual moments and, consequently, cannot couple to radiation (commonly known as *dark modes* [38,39]). Therefore, because we are concerned with exciting the metasurface with an incident field, here we work with the discretized versions that have antinodes at the metal regions, which are capable of coupling to radiation (commonly known as *bright modes* [39,40]). The strong near fields extend outside the dielectric slab region enabling sufficient coupling with the chiral layer we desire to probe, which we place on the slab. The chiral layer has thickness 50 nm, refractive index $n = 1.5 - 0.001i$, and chirality parameter $\kappa = 10^{-5}$ (realistic chirality parameter value of, e.g., aqueous solutions of monosaccharides [41,42] or biomolecules [10,19,43]). The whole system is placed on a glass substrate of refractive index $n = 1.5$, and the space on the opposite side (adjacent to the chiral layer) is index matched with the substrate. To maximize the interaction of the TE_{20} and TM_{20} bright modes with the chiral system, we adjust the width of the metal w to tune the modes at a common frequency, which for $w = 140$ nm is ~ 230 THz [Fig. 1(c), open symbols]. For our numerical simulations we perform full-wave vectorial finite element method (FEM) simulations, with the commercial software COMSOL MULTIPHYSICS [44].

We wish to add here that in this paper we choose to probe the chiral inclusion using the bright version of both the electric mode and the magnetic mode. Notwithstanding this, the dark counterparts of the two modes, which are nonradiative, can sustain stronger oscillations as compared with their bright versions (dissipation is only due to material absorption), and as such they could potentially lead to stronger chiroptical signals. However, bright modes can be directly excited by the interrogating beam, whereas, to use the dark modes under external excitation, we would have to break their symmetry in order to allow some coupling into the incident wave. To overcome this limitation, one could adopt the approach followed in Refs. [38–40], where a small dielectric scatterer is used to outcouple the energy stored in the dark mode of a metasurface laser. Then, under this approach, controllable outcoupling could be introduced, opening the possibility for even stronger signals, further tunability, and alternative implementations. However, such a possibility is far from the scope of this work, and we will examine it in future works.

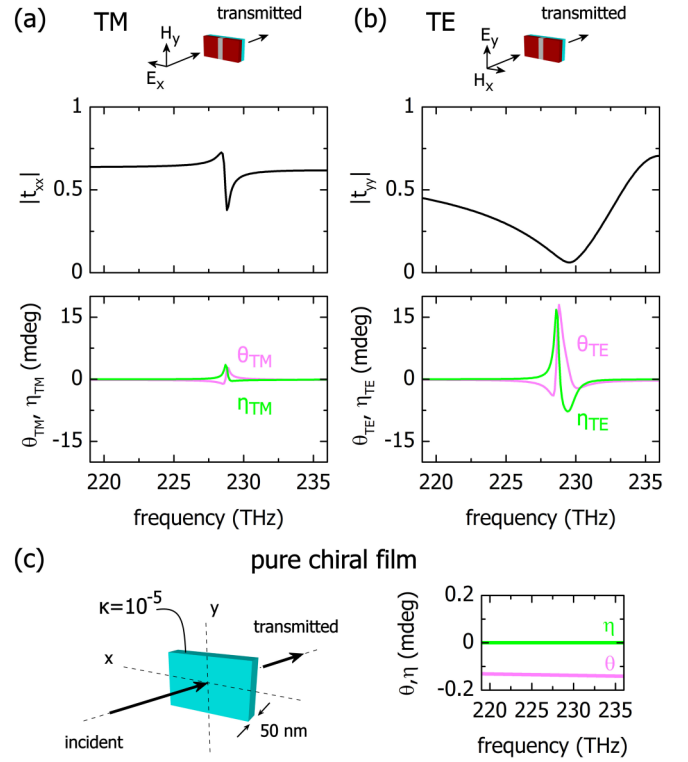


FIG. 2. Absolute values of cotransmission amplitudes and chiroptical signals θ (magenta lines) and η (green lines) for a chiral film with $\kappa = 10^{-5}$ (purely real) under (a) TM illumination and (b) TE illumination. In (c) the equivalent signals are shown for the pure chiral film, i.e., with the metasurface removed.

III. COMPLETE MEASUREMENT WITH TM AND TE LINEARLY POLARIZED BEAMS

To examine the role of anisotropy in our chiral sensing protocol, we investigate the response of the anisotropic metasurface under illumination with x - and y -linearly-polarized waves. First, with $\kappa = 0$, a x - (y -)polarized incident wave excites the TM_{20} (TE_{20}) mode, which cannot couple to the orthogonal TE_{20} (TM_{20}) mode, resulting in the copolarized scattering amplitudes t_{xx} , t_{yy} , r_{xx} , r_{yy} ; the subscripts in $t_{out,inc}$ and $r_{out,inc}$ denote the output and incident E -field polarization, respectively. Next, we set $\kappa = 10^{-5}$ and repeat the two experiments: Illumination with an x - (y -)polarized wave again leads to the excitation of the TM_{20} (TE_{20}) mode; however, due to chirality, the two modes can couple, giving rise to polarization conversion, which is identified in the cross-polarized scattering amplitudes t_{yx} , r_{yx} (t_{xy} , r_{xy}). Note that for the chosen (weak) $\kappa = 10^{-5}$, the copolarized scattering amplitudes (t_{xx} , t_{yy} , r_{xx} , r_{yy}) remain practically unchanged. To detect the effect of chirality on the incident wave, we analyze the polarization of the transmitted wave in terms of its rotation θ and ellipticity η .

In Fig. 2(a), we show the absolute value of the cotransmission amplitude t_{xx} (top panel) and the retrieved chiroptical, θ and η , signals (bottom panel) for x -linearly-polarized illumination. Similarly, in Fig. 2(b) we show the absolute value of the cotransmission amplitude t_{yy} and the retrieved chiroptical signals (bottom panel) for y -linearly-

polarized illumination. We refer to the illumination with $\mathbf{E} \parallel \hat{x}$ ($\mathbf{E} \parallel \hat{y}$) as TM (TE) illumination, to emphasize the fact that this particular polarization directly couples with the TM_{20} (TE_{20}) mode. It is evident that, in comparison with isotropic systems [17–19,23,27,30], anisotropy offers an additional degree of freedom in terms of the transmitted power ($|t_{xx}|^2$ or $|t_{yy}|^2$) and the attainable chiroptical signals. For example, for this particular system, one can choose between strong chiroptical signals $\theta_{\text{TE}}, \eta_{\text{TE}}$ on a relatively weak output beam [Fig. 2(b)] and somewhat weaker chiroptical signals $\theta_{\text{TM}}, \eta_{\text{TM}}$ on a significantly stronger output beam [Fig. 2(a)]. For both choices of illumination, the chiroptical signals are 30–100 times stronger than those from the chiral film alone, as shown in Fig. 2(c) ($\theta = 0.14$ mdeg and $\eta = 0$ at 230 THz).

A. Analysis of far-field chiroptical signals

In the examples of Figs. 2(a) and 2(b), what is being probed by the incident wave is not the chiral inclusion alone, but rather the composite system of the chiral inclusion with the metasurface. Therefore, to be able to retrieve κ , the chirality parameter of the chiral inclusion, it is necessary that we deconvolve the contributions from both subsystems. To gain insight into how the two subsystems contribute to the total chiroptical signals, we start with studying the far-field response of the composite system in terms of its effective material parameters. Because the metasurface is electrically thin, we can replace the entire composite system by a thin polarizable sheet (zero thickness) and work with equivalent surface quantities (sheet conductivities). Following a procedure similar to that used with isotropic metasurfaces [27], the transmission amplitudes can be expressed in terms of the effective surface (sheet) conductivities as (see SM [36] for details)

$$t_{xx} = \frac{1 - s_{ee}^{xx} s_{mm}^{yy}}{(1 + s_{ee}^{xx})(1 + s_{mm}^{yy})}, \quad (1a)$$

$$t_{yy} = \frac{1 - s_{ee}^{yy} s_{mm}^{xx}}{(1 + s_{ee}^{yy})(1 + s_{mm}^{xx})}, \quad (1b)$$

$$t_c = \frac{\sigma_c^{xx}}{2(1 + s_{ee}^{xx})(1 + s_{mm}^{xx})} + \frac{\sigma_c^{yy}}{2(1 + s_{ee}^{yy})(1 + s_{mm}^{yy})}, \quad (1c)$$

where $t_c \equiv t_{xy} = -t_{yx}$. In these expressions, $s_{ee}^{\alpha\alpha} = \zeta \sigma_{ee}^{\alpha\alpha}/2$ and $s_{mm}^{\alpha\alpha} = \sigma_{mm}^{\alpha\alpha}/2\zeta$, with $\alpha = \{x, y\}$, are the normalized (dimensionless) effective sheet conductivities corresponding to the electric mode and the magnetic mode of the metasurface alone, respectively, i.e., in the absence of chirality (for $\kappa = 0$); $\zeta = \sqrt{\mu_0 \mu / \epsilon_0 \epsilon}$ is the wave impedance of the surroundings. The (dimensionless) effective sheet conductivity $\sigma_c^{\alpha\alpha}$ of the composite system arises from the magnetoelectric coupling between the two, otherwise orthogonal, modes TM_{20} and TE_{20} , which is induced by the chiral film. As such, $\sigma_c^{\alpha\alpha}$ contains contributions from both the chiral inclusion and the metasurface, i.e., from κ , s_{ee} , and s_{mm} . With the aid of Eqs. (1a)–(1c) we see that the resonant response of the metasurface alone (captured by the effective material parameters s_{ee}, s_{mm}) is involved in all transmission amplitudes, whereas the chirality κ of the chiral inclusion (captured by the effective material parameter σ_c) appears only in the cross-polarized transmission amplitude t_c . In view of this observation, a dis-

tinct advantage of anisotropic metasurfaces becomes evident: Because anisotropy allows for the independent control of the sheet conductivities along the different x, y axes, we can independently tune the cotransmission and cross-transmission amplitudes and, likewise, the chiroptical signals. This can be achieved by designing the electric and magnetic modes along both directions, in turn, by tuning $s_{ee}^{xx}, s_{ee}^{yy}, s_{mm}^{xx}, s_{mm}^{yy}$. For example, note how in Eq. (1a) t_{xx} changes only with s_{ee}^{xx}, s_{mm}^{yy} whereas all $s_{ee}^{xx}, s_{mm}^{yy}, s_{ee}^{yy}, s_{mm}^{xx}$ are involved in the cross-polarized term t_c ; the additional conductivities s_{ee}^{yy}, s_{mm}^{xx} can be used to tune θ, η independently from the transmittance t_{xx} , which remains unchanged. This gives an additional degree of freedom to maximize the chiroptical signals for a certain achievable transmittance. Similarly, the same conclusions hold for simpler systems, as in our example, where TE_{20} and TM_{20} provide resonant conductivities along the y axis only, and s_{ee}^{xx}, s_{mm}^{xx} are practically constant across the entire spectral range of interest (see SM [36]); notice how, e.g., upon TM illumination, t_{xx} is tuned via s_{mm}^{yy} , while t_c is tuned via both s_{mm}^{yy} and s_{ee}^{yy} .

To quantify the observed tunability, we proceed with expressing the chiroptical signals θ and η in terms of t_{xx}, t_{yy} , and t_c . With the aid of the Stokes parameters we find for weak cross-polarization conversion ($t_c \ll t_{xx}, t_{yy}$)

$$\theta_{\text{TM/TE}} = \text{Re}\left(-\frac{t_c}{t_{xx/yy}}\right), \quad (2a)$$

$$\eta_{\text{TM/TE}} = \text{Im}\left(-\frac{t_c}{t_{xx/yy}}\right). \quad (2b)$$

Equations (2a) and (2b) illustrate how the chiroptical signals θ, η can be in general different between the two polarizations. This is in contrast to the case for isotropic metasurfaces [27], where the chiroptical signals are the same for both x - and y -linearly-polarized waves and inversely proportional to the cotransmission amplitude $t \equiv t_{xx} = t_{yy}$. Therefore the ability to independently tune the cotransmission and cross-transmission amplitudes, by choosing different excitations, allows us to control the (enhanced) chiroptical signals, as we demonstrate in Fig. 2. We emphasize once again that such a capability is not feasible in isotropic metasurfaces. The numerically calculated chiroptical signals in Fig. 2 are also in agreement with their analytical form, as given by Eqs. (2a) and (2b), which we verify by separately calculating the ratios t_c/t_{xx} and t_c/t_{yy} and comparing their real and imaginary parts with $\theta_{\text{TM/TE}}, \eta_{\text{TM/TE}}$ (see SM [36]).

Last, we note here that due to the relatively weak chirality, $\sigma_c^{xx}, \sigma_c^{yy} \propto \kappa$ (see SM [36]) and, consequently, $t_c \propto \kappa$ [see Eq. (1c)]. Therefore, in view of Eqs. (2a) and (2b), the far-field chiroptical signals $\theta_{\text{TM/TE}}, \eta_{\text{TM/TE}}$ are directly proportional to κ , and therefore measurements of θ, η are expected to be sensitive to both $|\kappa|$ and $\text{sgn}(\kappa)$, and to both $\text{Re}(\kappa)$ and $\text{Im}(\kappa)$. This can be easily seen if we allow κ to be dispersive, as we do next.

B. Determination of unknown chirality

To deduce the chirality parameter κ of an unknown chiral inclusion, in most relevant experiments [17–19,23,25,26,29–32], chiral sensing relies on measurements in transmission

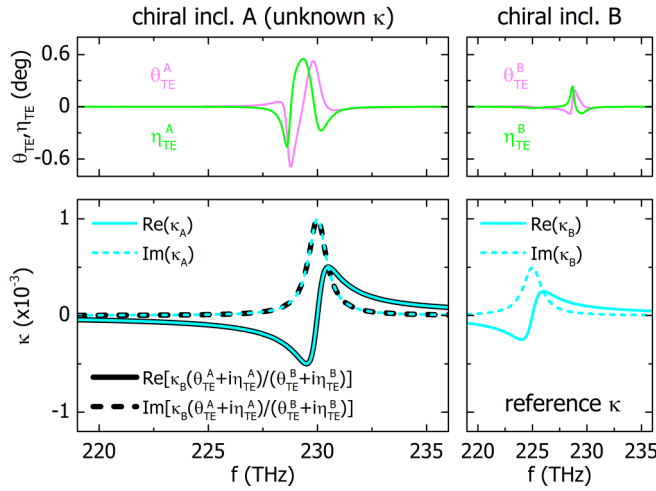


FIG. 3. Retrieval of the chirality parameter κ_A of an unknown inclusion (incl.) A, using a reference chirality parameter κ_B of inclusion B, and the chiroptical signals θ_{TE} , η_{TE} in transmission. Top row: numerically calculated chiroptical signals θ_{TE} , η_{TE} for each inclusion. Bottom row: chirality parameters κ_A , κ_B of the two inclusions (cyan lines) and retrieved κ_A (black lines) of inclusion A.

only, naturally raising the question of how this can be also implemented in the framework of anisotropic metasurfaces. As we show next, this is possible if we use the rotation θ and ellipticity η of the transmitted wave.

According to the results of Eqs. (2a) and (2b), $\theta_{TM/TE}$ and $\eta_{TM/TE}$ are the real and imaginary parts, respectively, of the same quantity, i.e., $-t_c/t_{xx/yy}$. Therefore we may combine the two expressions in each of Eqs. (2a) and (2b) and solve for t_c , to obtain

$$t_c = -(\theta_{TM/TE} + i\eta_{TM/TE}) \cdot t_{xx/yy}. \quad (3)$$

With the result of Eq. (3) we are now able to unambiguously determine an unknown chirality solely from the chiroptical signals θ , η in transmission. To see how this is possible, let us consider two chiral inclusions, A and B, which we probe with our system under TM or TE illumination. The chiroptical signals $\theta_{TM/TE}^A$, $\eta_{TM/TE}^A$, and $\theta_{TM/TE}^B$, $\eta_{TM/TE}^B$, obtained either from simulations or experiments using inclusions A and B, respectively, correspond to the individual transmission amplitudes t_c^A and t_c^B , according to Eq. (3). Taking into account that $t_c \propto \kappa$, we can divide t_c^A and t_c^B to eliminate the common $t_{xx/yy}$ term and express an unknown chirality parameter, here κ_A , in terms of a reference one, here κ_B , as

$$\kappa_A = \kappa_B \cdot \frac{\theta_{TM/TE}^A + i\eta_{TM/TE}^A}{\theta_{TM/TE}^B + i\eta_{TM/TE}^B}. \quad (4)$$

This procedure is illustrated in Fig. 3 for TE illumination and two inclusions A and B with chirality parameters κ_A and κ_B , respectively, of the form [3,27,45]

$$\kappa_{A/B}(\omega) = \frac{\omega_{\kappa,A/B}\omega}{\omega_{0\kappa,A/B}^2 - \omega^2 + i\gamma_{\kappa,A/B}\omega}. \quad (5)$$

We emphasize here that, in contrast to our previous examples where κ is constant, here we consider the (realistic) case of dispersive chirality. In this example, for inclusion A we use $\omega_{\kappa,A} = 2\pi \times 1 \times 10^{-3}$ THz, $\omega_{0\kappa,A} = 2\pi \times 230$ THz, and

$\gamma_{\kappa,A} = 2\pi \times 1$ THz, and for inclusion B we use $\omega_{\kappa,B} = 2\pi \times 1 \times 10^{-3}$ THz, $\omega_{0\kappa,B} = 2\pi \times 225$ THz, and $\gamma_{\kappa,B} = 2\pi \times 2$ THz, to demonstrate that we can accurately determine the chirality of the (unknown) chiral inclusion A, i.e., the true value of κ_A , using a chiral inclusion of known chirality parameter (κ_B) and comparing their respective chiroptical signals, obtained using transmission measurements under TE or TM illumination. In Fig. 3 (top row) we present the chiroptical signals θ_{TE} , η_{TE} for the two, known and unknown, chiral inclusions. We also present in Fig. 3 (bottom row) the chirality parameters of the two inclusions together with the (accurately) retrieved chirality for inclusion A using the chiroptical signals, as dictated by Eq. (4). The same result can also be recovered with TM illumination (see SM [36]). We emphasize here that, with our example, we demonstrate the validity of Eq. (4) in providing the entire spectral response of an unknown chiral inclusion even for cases of unknown chiral inclusions with high chirality values (in our example, on the order of $\sim 10^{-3}$ on resonance).

The result of Eq. (4) is particularly practical for experiments and applications as it allows for direct determination of the chirality parameter κ of an unknown chiral substance with measurements solely in transmission (and with the aid of a calibration measurement). This eliminates the need for (i) knowing both the reflection and transmission amplitudes and (ii) extracting the effective conductivities in an intermediate step. Most importantly, with this procedure we manage to effectively deconvolve the dispersion of the metasurface from the dispersion of the chiral inclusion and obtain the pure spectral response κ of the chiral inclusion.

IV. COMPLETE MEASUREMENT WITH ELLIPTICALLY POLARIZED BEAMS

The anisotropy of our system allows us to gain access to stronger chiroptical signals by using elliptically polarized incident waves, an additional functionality not feasible in isotropic systems [26]. To demonstrate this, we start by parametrizing the elliptically polarized incident wave as

$$\mathbf{E}_{\text{inc}} = \begin{pmatrix} E_{0x}\hat{x} \\ E_{0y}\hat{y} \end{pmatrix} = \begin{pmatrix} E_0 \cos \phi_{\text{rot}}\hat{x} \\ E_0 \sin \phi_{\text{rot}}e^{i\phi_{\text{lag}}}\hat{y} \end{pmatrix}, \quad (6)$$

where the angle ϕ_{rot} is the angle between the incident wave's E field and the x axis and ϕ_{lag} tunes the phase lag between the x and y wave components; E_0 is a complex constant. By tuning ϕ_{rot} and ϕ_{lag} we gain access to any desired polarization. Of course, because the metasurface is anisotropic (birefringent), any incident polarization that is not parallel or vertical to the metal wires (equivalent to the fast or slow axis of typical anisotropic systems) will result in θ , η signals, even for $\kappa = 0$; therefore, for $\kappa \neq 0$, the θ , η signals may contain achiral background contributions from the metasurface itself that may hinder accurate chirality measurements. In this case, subtraction of the (achiral) background contribution is required, and this could be realized using two different approaches: performing measurements with and without the chiral layer (similarly to the work of Ref. [25]) or implementing a signal reversal that allows us to isolate the signal from the chiral inclusions. Next, we examine both approaches individually.

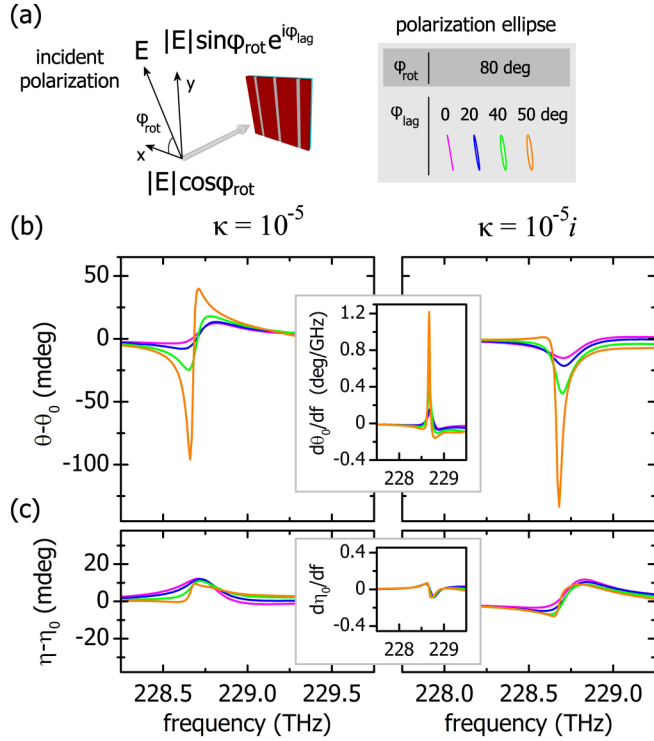


FIG. 4. Enhanced chiral sensing using an elliptically polarized incident wave. (a) Incident polarization and polarization ellipse for selected examples. Subtraction of far-field measurements of optical rotation and ellipticity in the presence and absence of the chiral layer, i.e., (b) $\theta - \theta_0$ and (c) $\eta - \eta_0$, for the selected polarizations shown in (a); $\kappa = 10^{-5}$ (left panels), $\kappa = 10^{-5}i$ (right panels). For $\phi_{\text{rot}} = 80^\circ$, $\phi_{\text{lag}} = 50^\circ$, the optical rotation signal is enhanced by a factor of more than ~650 compared with the respective signal of a pure chiral film with $\kappa = 10^{-5}$.

A. Measurements in transmission with background subtraction

In Fig. 4 we show the first possibility for a constant chirality parameter $\kappa = 10^{-5}$. In particular, for fixed $\phi_{\text{rot}} = 80^\circ$, as we increase ϕ_{lag} [Fig. 4(a)] we find that the difference between two measurements with and without the chiral layer, i.e., $\theta - \theta_0$ [where θ (θ_0) is with (without) the chiral layer], increases and becomes maximum for $\phi_{\text{lag}} = 50^\circ$. For this illumination we obtain enhanced chiroptical signals by a factor of more than ~650 compared with the respective signal from the pure chiral film (~0.14 mdeg) [Fig. 2(c)], as we show in Fig. 4(b). Additionally, in Figs. 4(b) and 4(c) we demonstrate the ability with such a subtraction procedure to acquire pure chiroptical signals for the case of (purely imaginary) $\kappa = 10^{-5}i$.

The strong enhancement of the chiroptical signals [Figs. 4(b) and 4(c)] originates from the anisotropy of the metasurface; under illumination with an elliptically polarized beam, the chiroptical signals change as $\theta - \theta_0 \sim d\theta_0/df$ and $\eta - \eta_0 \sim d\eta_0/df$, where f is the frequency [26]. Essentially, the chiroptical signals due to the chiral inclusions are significantly enhanced at frequency ranges where the metasurface's anisotropy changes abruptly (i.e., the derivatives of θ_0 , η_0 become large). This is illustrated in the insets of Figs. 4(b) and 4(c), where the calculated derivatives $d\theta_0/df$ and $d\eta_0/df$ with the chiral layer removed are proportional to $\theta - \theta_0$ and $\eta - \eta_0$, respectively.

B. Measurements in transmission using a signal reversal: Absolute measurements

Removing the chiral inclusion to subtract the background signals may result in unintentional changes in the measurement setup. This can possibly affect the measurement accuracy, and therefore it would be useful to be able to perform chirality measurements without the need for sample removal.

Our system offers the possibility for absolute measurements by means of a crucial signal reversal with which one can directly isolate the (enhanced) chiroptical signal without the need for sample removal and interference with the system, a unique approach in metamaterial-based chiral sensing schemes: Excitation with reversed polarization yields separate polarization effects of opposite sign, thus enabling the isolation of signals originating only from the chiral inclusion. According to our parametrization of Eq. (6), this can be realized by reversing ϕ_{rot} upon illumination, yielding different chiroptical signals with opposite rotations and ellipticities that we label as θ_{\pm} and η_{\pm} . By taking their mean value, i.e., $2\Delta\theta_{\text{rev}} \equiv \theta_+ + \theta_-$ and $2\Delta\eta_{\text{rev}} \equiv \eta_+ + \eta_-$, any signal originating from the metasurface is canceled, as well as any other potential achiral backgrounds, while the pure chiroptical signal, which is even under this polarization reversal, doubles. Thus the importance of the signal reversal becomes apparent: Under realistic experimental conditions, one can appropriately tune the frequency of the probing radiation around the resonance of the metasurface and apply this reversal (e.g., with the use of polarization modulators), isolating the chiral signal even in the presence of high-noise environments and other achiral effects (generally, signal reversals have been crucial for enabling sensitive measurements of circular birefringence in conditions where traditional polarimetry fails to perform [41,42,46]).

The average signals $\Delta\theta_{\text{rev}}$ and $\Delta\eta_{\text{rev}}$ can be expressed as (see SM [36] for derivation)

$$\Delta\theta_{\text{rev}} = \text{Re} \left(-t_c \frac{c_{\text{rot}}^2 t_{xx} + s_{\text{rot}}^2 t_{yy} e^{2i\phi_{\text{lag}}}}{c_{\text{rot}}^2 t_{xx}^2 + s_{\text{rot}}^2 t_{yy}^2 e^{2i\phi_{\text{lag}}}} \right), \quad (7a)$$

$$\Delta\eta_{\text{rev}} = \text{Im} \left(-t_c (c_{\text{rot}}^2 t_{xx}^* + s_{\text{rot}}^2 t_{yy}^*) \frac{|c_{\text{rot}}^2 t_{xx}^2 + s_{\text{rot}}^2 t_{yy}^2 e^{2i\phi_{\text{lag}}}|}{(c_{\text{rot}}^2 |t_{xx}|^2 + s_{\text{rot}}^2 |t_{yy}|^2)^2} \right. \\ \left. + \frac{\text{Re} \{ t_c (t_{xx} - t_{yy}) (c_{\text{rot}}^2 e^{-i\phi_{\text{lag}}} t_{xx}^2 + s_{\text{rot}}^2 e^{i\phi_{\text{lag}}} t_{yy}^2)^* \} 2c_{\text{rot}}^2 s_{\text{rot}}^2 e^{-i\phi_{\text{lag}}} t_{xx} t_{yy}^*}{(c_{\text{rot}}^2 |t_{xx}|^2 + s_{\text{rot}}^2 |t_{yy}|^2)^2 |c_{\text{rot}}^2 t_{xx}^2 + s_{\text{rot}}^2 t_{yy}^2 e^{2i\phi_{\text{lag}}}|} \right), \quad (7b)$$

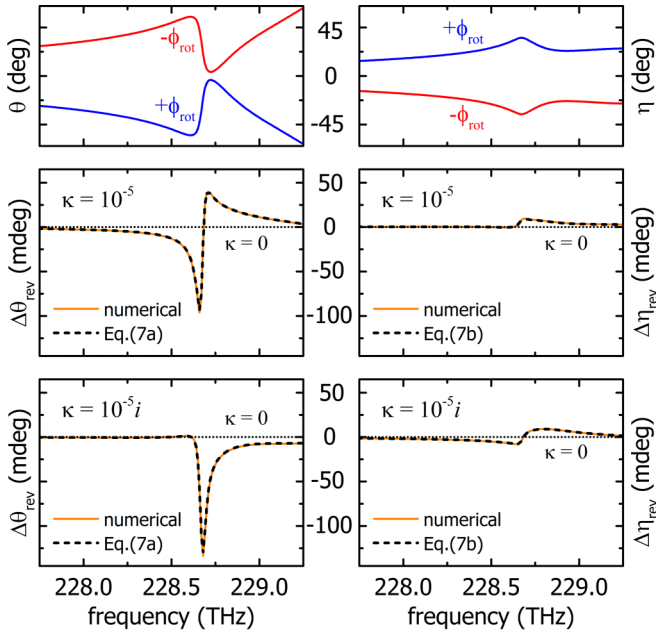


FIG. 5. Absolute measurement of real- and imaginary-valued chirality parameter κ with polarization reversal of an elliptically polarized incident wave. Top panels: Measurements for $\phi_{\text{lag}} = 50^\circ$ with $\phi_{\text{rot}} = \pm 80^\circ$, appearing to be similar for the cases of $\kappa = 10^{-5}$ and $\kappa = 10^{-5}i$ (note that these signals are approximately three orders of magnitude stronger than the pure chiroptical signals). Middle and bottom panels: The independent measurements shown in the top panels are averaged to yield different chiroptical signals $\Delta\theta_{\text{rev}}$, $\Delta\eta_{\text{rev}}$ (orange lines), for $\kappa = 10^{-5}$ (middle panels) and $\kappa = 10^{-5}i$ (bottom panels). The analytical plots of Eqs. (7a) and (7b) for the respective cases are also shown (black dashed lines). Dotted lines show $\kappa = 0$.

where $c_{\text{rot}} = \cos(\phi_{\text{rot}})$, $s_{\text{rot}} = \sin(\phi_{\text{rot}})$, and t_{xx}, t_{yy}, t_c are the transmission amplitudes obtained with TE and TM linearly polarized illumination. Because t_{xx}, t_{yy}, t_c do not depend on $\phi_{\text{rot}}, \phi_{\text{lag}}$, the form of Eq. (7a) implies that there is always a combination of $\phi_{\text{rot}}, \phi_{\text{lag}}$ that can minimize and possibly eliminate the denominator entirely, thus enhancing $\Delta\theta_{\text{rev}}$, as we demonstrate in Fig. 4. On the other hand, because the denominator in Eq. (7b) involves sums of positive quantities, a similar conclusion cannot be drawn directly for $\Delta\eta_{\text{rev}}$.

To illustrate these observations, in Fig. 5 we present simulations of θ and η for incident elliptical waves with $\phi_{\text{rot}} = \pm 80^\circ$ and $\phi_{\text{lag}} = 50^\circ$, which are averaged ($\Delta\theta_{\text{rev}}, \Delta\eta_{\text{rev}}$) to yield signals originating only from the chiral inclusions (we perform the calculations for the cases of purely real-valued and purely imaginary-valued chirality parameters, $\kappa = 10^{-5}$ and $\kappa = 10^{-5}i$, respectively). In Fig. 5 we also present the analytical plots of Eqs. (7a) and (7b) (dashed lines), for which we use t_{xx}, t_{yy} with $\kappa = 0$ and t_c with $\kappa = 10^{-5}$, from the simulations. Note that our results are also in agreement with the measurements we present in Fig. 4, where the signals originating from the chiral inclusions are obtained via a background subtraction procedure.

C. Sensitivity on polarization reversal errors

Absolute chiral sensing using the proposed signal reversal requires the ability to precisely control the polarization state

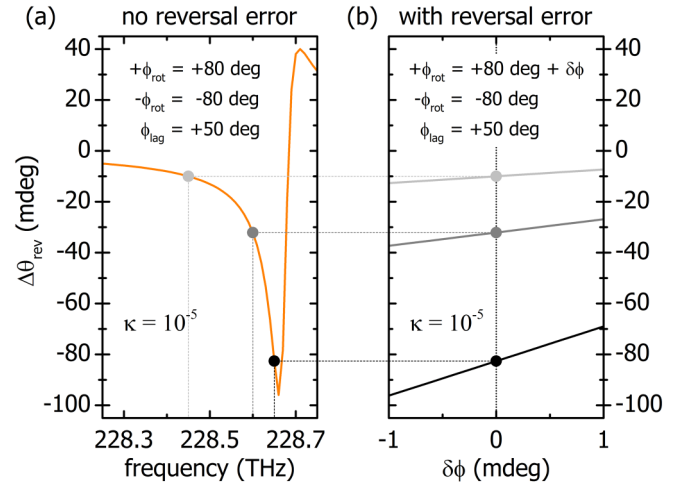


FIG. 6. Dependence of chiroptical rotation signal on polarization reversal errors (i.e., measurement sensitivity). (a) Averaged signal $\Delta\theta_{\text{rev}}$ for the case of $\kappa = 10^{-5}$ with $\delta\phi = 0$. (b) Averaged signal $\Delta\theta_{\text{rev}}$ as a function of $\delta\phi$ for the selected operation points marked in (a).

of the incident beam [accurate tuning of the principal axis of the polarization state (ϕ_{rot}) and the ellipticity (ϕ_{lag})] for sensitive measurements. In our scheme, to apply the polarization reversal, it suffices to fix ϕ_{lag} and then reverse ϕ_{rot} as we demonstrate in Figs. 4 and 5; that is, it is not required to manipulate both ϕ_{rot} and ϕ_{lag} simultaneously. In practical implementations, however, reversal imperfections may affect the measurement precision.

To quantify such a possibility, we introduce a reversal error, $\delta\phi$, as $+\phi_{\text{rot}} + \delta\phi$ and $-\phi_{\text{rot}}$, and we repeat the measurements of $\Delta\theta_{\text{rev}}$ of Fig. 5 [$\kappa = 10^{-5}$ and $\phi_{\text{rot}} = \pm 80^\circ$, $\phi_{\text{lag}} = 50^\circ$]. In Fig. 6(a) we show the chiroptical rotation signal after the application of the signal reversal, $\Delta\theta_{\text{rev}}$, for $\delta\phi = 0$, and in Fig. 6(b) we show $\Delta\theta_{\text{rev}}$ as a function of $\delta\phi$ for a few selected operation (frequency) points [as marked in Fig. 6(a)]. We observe that the measurement's sensitivity in the reversal error $\delta\phi$ increases with signal strength, which is expected as the latter changes as $\sim d\theta_0/df$. In particular, for $|\delta\phi| \sim 1$ mdeg we observe deviations of several millidegrees in the measured signal (depending on the operational or measurement frequency), and these increase as we approach the frequency where the metasurface's anisotropy changes abruptly. Notwithstanding this, the sensitivity limit of any polarimetric (optical) measurement is ultimately defined by the photon shot noise [which for ~ 1 mW of laser radiation at ~ 1310 nm (~ 229 THz) is at the sub- $\mu\text{deg}/\sqrt{\text{Hz}}$ level], and even in the case of commercially available optical spectropolarimeters, polarimetric sensitivities can reach $< 100\text{-}\mu\text{deg}$ levels. As such, signal-reversal control is feasible with high accuracy and precision (i.e., $\delta\phi < 0.1$ mdeg), ensuring the ability to perform sensitive absolute chiral sensing using our proposed signal reversal.

D. Determination of unknown chirality with measurements in transmission

In experiments it would be particularly useful to have a calibration scheme for measurements with elliptical polariza-

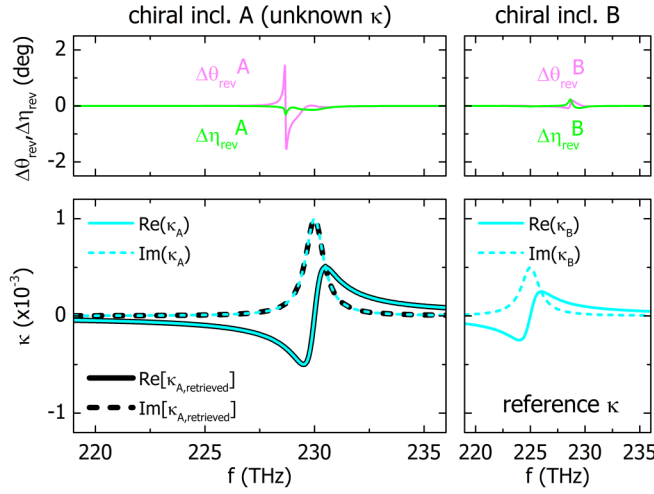


FIG. 7. Retrieval of the chirality parameter κ_A of an unknown inclusion A, using a reference chirality parameter κ_B of inclusion B and an elliptically polarized beam with $\phi_{\text{rot}} = \pm 80^\circ$, $\phi_{\text{lag}} = 50^\circ$. Top row: numerically calculated chiroptical signals $\Delta\theta_{\text{rev}}$, $\Delta\eta_{\text{rev}}$ for each inclusion. Bottom row: chirality parameters κ_A , κ_B of the two chiral inclusions (cyan lines) and retrieved κ_A (black lines) of inclusion A, using the reference values of κ_B and the chiroptical signals $\Delta\theta_{\text{rev}}$, $\Delta\eta_{\text{rev}}$.

tion, similar to the case of TM or TE illumination, where an unknown chirality κ_A is determined in terms of a reference chirality κ_B . Previously, the simple form of Eq. (4) was derived on the basis that the rotation θ and ellipticity η are the real and imaginary parts of the same complex quantity, which is proportional to κ [see Eqs. (2a) and (2b)]. Although, under elliptical illumination, $\Delta\theta_{\text{rev}}$ and $\Delta\eta_{\text{rev}}$ are the real and imaginary parts of different complex quantities [see Eqs. (7a) and (7b)], as we show in the SM [36], it is still possible to obtain the unknown chirality in a similar form, as

$$\kappa_A = \kappa_B \frac{\Delta\theta_{\text{rev}}^A + g\Delta\eta_{\text{rev}}^A}{\Delta\theta_{\text{rev}}^B + g\Delta\eta_{\text{rev}}^B}, \quad (8)$$

where g is a function of the angles ϕ_{rot} , ϕ_{lag} characterizing the elliptical polarization and the cotransmission amplitudes t_{xx} and t_{yy} obtained previously with TM and TE illumination, respectively. The result of Eq. (8) generalizes Eq. (4) for any arbitrary incident polarization. Indeed, for $\phi_{\text{rot}} = 0$ (TM illumination) or $\phi_{\text{rot}} = \pi/2$ (TE illumination), $g = i$ and Eq. (8) reduces to Eq. (4). As an example, in Fig. 7 we use Eq. (8) to retrieve the unknown chirality κ_A in terms of the reference chirality κ_B using elliptically polarized illumination with $\phi_{\text{rot}} = \pm 80^\circ$, $\phi_{\text{lag}} = 50^\circ$. For κ_A , κ_B we use the parameters previously used in Fig. 3 to demonstrate the equivalent retrieval with TE illumination.

Finally, we wish to add that, with the introduction of an additional reference chirality κ_C , we can also retrieve the unknown chirality entirely in terms of the $\Delta\theta$, $\Delta\eta$ signals of the three molecules, i.e., without the need to involve the angles ϕ_{rot} , ϕ_{lag} and the cotransmission amplitudes t_{xx} , t_{yy} (see SM [36] for details).

V. BROADBAND OPERATION

The operational spectral range of our metasurface depends on the properties of the utilized resonant modes; altering those, one can selectively tune the metasurface's operation frequency to approach that, for instance, of a target substance. For our proposed design, we can tune the operation of the metasurface over a wide spectral range—from near-ultraviolet (NUV) to near-infrared (NIR) frequencies—coarsely and finely by changing the properties of the materials forming the metasurface and its geometric characteristics, respectively. Particularly, in Ref. [26] we have chosen specific metasurface design parameters for operation at visible frequencies [370 THz (800 nm)], while in this paper we select design parameters for operation at near-infrared frequencies [230 THz (1300 nm)].

Considering this general design principle, we can see how our system can be implemented for chiroptical spectroscopy over different spectral ranges with the capacity for wide spectral coverage. For this reason, we present here two particular designs: (i) one suitable for broadband spectral coverage in the visible and near infrared on a single platform and (ii) one suitable for operation at near-ultraviolet frequencies.

A. Pixelated sensor for operation in the visible and near infrared

For broadband spectral coverage in the visible and near infrared we visualize a pixelated chiral sensor, as shown in Fig. 8(a), where each *metapixel* is dedicated to the detection of chirality at a particular spectral range, following a principle of operation similar to that of the recently demonstrated imaging-based molecular barcoding enabled by high- Q dielectric resonators for the detection of midinfrared molecular fingerprints [47]. To develop such a sensor, we start by selecting a design for operation at a particular frequency range, and to span a broad spectral range, we finely tune the design parameters to change the resonant frequencies of the TE_{20} and TM_{20} modes assigning, thus, a new metapixel to the overall design. By repeating this procedure we can cover practically any desired spectral range.

As an example, in Fig. 8 we demonstrate a system for operation at ~ 770 - 920 nm (spanning a range of ~ 70 THz). In particular, we start with designing the system for operation at 800 nm (374 THz), and we use a slab with refractive index $n_{\text{slab}} = 2.52$ (e.g., TiO_2) and thickness $t_d = 80$ nm on a glass substrate with $n = 1.45$. The metallic wires are made of silver (Ag) and are placed on one side of the dielectric slab, as illustrated in the schematic of Fig. 8(a) [26]. The wire cross section on the xz plane has thickness 50 nm and width 80 nm, and the wire periodicity is $\alpha = 500$ nm. For the simulation we choose a chiral layer, which we place on the slab, of thickness $t_c = 50$ nm and refractive index $n_c = 1.33 - 10^{-4}i$, and the entire space above the chiral layer is water with $n = 1.33$. For TM excitation we obtain chiroptical rotation θ signals as large as 6.5 mdeg peak to peak, for a transmittance of $\sim 10\%$. As a comparison, the optical rotation signal from a transmission measurement of a 50-nm chiral layer with $\kappa = 10^{-5}$ at 800 nm is ~ 0.24 mdeg, achieving, thus, enhancements by a factor of ~ 27 [Fig. 8(b), insets]. For TE illumination or excitation with an elliptical beam we can further enhance

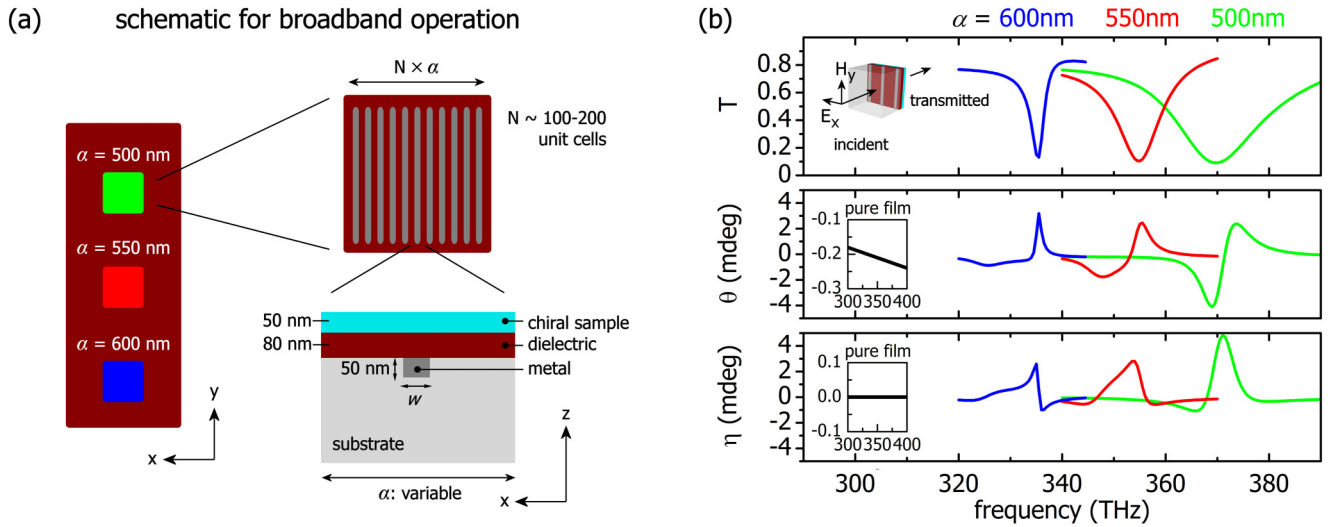


FIG. 8. Implementation for broadband operation. (a) Pixelated metasurface composed of a two-dimensional array of metaunits with resonant frequencies tuned over a wide spectral range (here, ~ 70 THz) to target, e.g., specific molecular spectral features. (b) Performance for TM illumination. For this example the metallic wires have constant width $w = 80$ nm and variable periodicity α , ranging from 500 to 600 nm, as shown.

our signals, even by an order of magnitude, as we show in Ref. [26].

To shift the operation at lower frequencies, we increase the periodicity of the metallic wires; by increasing the periodicity we shift the resonant frequencies of the electric and the magnetic mode to lower frequencies, and by changing the cross section of the metallic wires we can fine-tune the spectral overlap of the two modes. To demonstrate the versatility of our design, here we only change the periodicity α (all other material and geometrical parameters remain unchanged). In particular, for $\alpha = 550$ nm we can lower the operation by 20 THz (at 850 nm), and for $\alpha = 600$ nm we can further lower the operation by an additional 20 THz (at 900 nm). We see that, even for the case of solely tuning the wire periodicity, we can cover a broad spectral range and support chiroptical rotation θ signals as large as 4 mdeg peak to peak, for a transmittance of $\sim 10\%$.

Given the design shown in Fig. 8(a), then, for 100–200 unit cells per metapixel, and for a range of wire periodicities of, e.g., $\alpha = 450$ –700 nm, we can develop an overall design that enables chiroptical molecular spectroscopy over a broad spectral range (of more than 100 THz) on a sub- mm^2 device.

B. Near-ultraviolet operation

Most recent nanophotonic- or metamaterial-based chiral sensing platforms have been largely designed to operate at infrared and visible frequencies where materials (metals and dielectrics) have (typically) low losses, and hence most experimental demonstrations have been performed on large molecules that possess chiroptical bands at visible and infrared frequencies. However, for most (small) molecules, strong chiral absorption features are in the ultraviolet (UV) spectral region, and the ability to improve the performance of chiral sensing platforms in the UV can be pivotal [32].

We present in Fig. 9 a specific design of our metasurface platform that allows for enhanced chiroptical spectroscopy

at near-UV frequencies (~ 380 nm). To achieve operation at the desired spectral region, we modify the design of our previous example (Fig. 8) by replacing the slab and metallic wire material with Ta_2O_5 and Al, respectively, and by reducing the slab thickness to 40 nm and the wire periodicity to 260 nm; the wire cross section on the xz plane is modified to have thickness 40 nm and width 30 nm. The 50-nm chiral film is characterized by $\kappa = 10^{-5}$ and $n = 1.339 - 10^{-4}i$ (for water, $n = 1.339$ at ~ 400 nm), and the glass substrate has $n = 1.47$ [Fig. 9(a)]. Despite the relatively weak enhancement for TM illumination [Fig. 9(b)], we find that under elliptical illumination [Fig. 9(c)], the chiroptical rotation signal θ is enhanced by a factor of ~ 165 , compared with the respective signal for measuring the chiral film without the metasurface.

As one pursues a further increase in frequency (from the near UV to the UV), the choice of materials for the implementation of the proposed scheme becomes a challenging task. The reason is that in the UV several dielectrics become lossy and, in particular, many metals lose their metallic character. Other than that, and as we demonstrate with this example of operation at near-UV frequencies, our proposed scheme is general, and there is no fundamental limitation with respect to the operational spectral range.

VI. CONCLUSIONS

In this paper we analyzed the key functionalities and benefits of using anisotropic metasurfaces for metasurface-based enhanced chiral sensing. Our approach was based on using the chirality of the inclusion to be probed, in order to couple two orthogonal modes of the achiral metasurface that have parallel electric and magnetic components. As the use of two such modes is met in several other contemporary nanophotonic-based approaches, the key difference here is that our approach for enhanced chiral sensing is based on the anisotropic response of the metasurface, rather than the superchirality of the

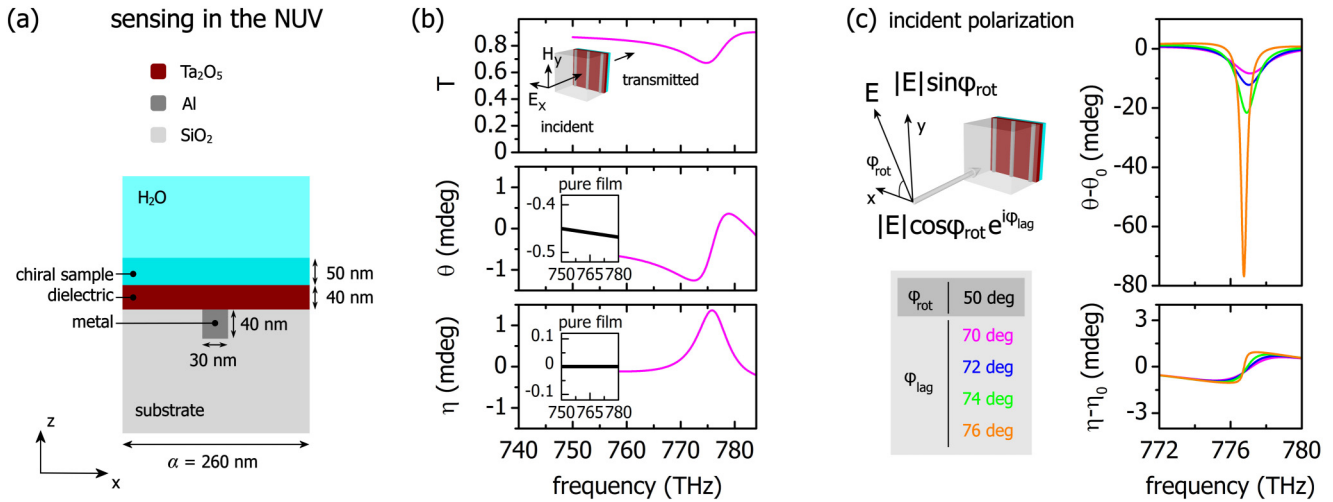


FIG. 9. Design for operation in the near ultraviolet (NUV). (a) Sample schematic. (b) Performance for TM illumination. (c) Performance for illumination with an elliptical beam. For TM illumination the chiroptical signals are enhanced by a factor of 2–3 [compared with single-pass transmission polarimetric measurements; insets in (b)], while under elliptical illumination the chiroptical rotation signal θ is enhanced by a factor of ~ 165 .

generated near fields. Owing to the unique benefits offered by anisotropy, our approach provides a platform where aspects crucial for chiral sensing in the nanoscale can be realized: (i) enhanced chiroptical signals by more than two orders of magnitude for ultrathin, subwavelength, chiral samples over a uniform and accessible area, (ii) complete measurements of the total chirality (magnitude and sign of both its real and imaginary parts), and (iii) measurements in an absolute manner, i.e., without the need for sample removal, due to the possibility of a crucial signal reversal (excitation with reversed polarization). We derived analytically, and verified numerically, simple formulas that provide insight into the sensing mechanism and explain how anisotropic metasurfaces offer additional degrees of freedom with respect to other isotropic metasurfaces. Importantly, our theoretical approach

provides a unified description of achiral anisotropic metasurfaces for chiral sensing that extends beyond the specific example systems we have used and can therefore motivate alternative designs. We demonstrated practical measurement schemes for the complete and unambiguous determination of an unknown chirality, and we provided the design principles towards broadband operation—from near-infrared to near-ultraviolet frequencies—opening the way for highly sensitive nanoscale chiroptical spectroscopy.

ACKNOWLEDGMENTS

We acknowledge the support of the European Commission Horizon 2020 ULTRACHIRAL Project (Grant No. FETOPEN-737071).

- [1] L. D. Barron, *Molecular Light Scattering and Optical Activity*, 2nd ed. (Cambridge University Press, Cambridge, 2004).
- [2] K. W. Busch and M. A. Busch, *Chiral Analysis* (Elsevier, Amsterdam, 2006).
- [3] E. U. Condon, Theories of optical rotatory power, *Rev. Mod. Phys.* **9**, 432 (1937).
- [4] I. V. Lindell, A. H. Sihvola, S. A. Tretyakov, and A. J. Viitanen, *Electromagnetic Waves in Chiral and Bi-isotropic Media* (Artech House, Norwood, 1994).
- [5] P. H. Vaccaro, Optical rotation and intrinsic optical activity, in *Comprehensive Chiroptical Spectroscopy* (Wiley, New York, 2011), Chap. 11, pp. 275–323.
- [6] Y. Tang and A. E. Cohen, Optical Chirality and Its Interaction with Matter, *Phys. Rev. Lett.* **104**, 163901 (2010).
- [7] G. Pellegrini, M. Finazzi, M. Celebrano, L. Duò, and P. Biagioni, Chiral surface waves for enhanced circular dichroism, *Phys. Rev. B* **95**, 241402(R) (2017).
- [8] S. Droulias and L. Bougas, Surface plasmon platform for angle-resolved chiral sensing, *ACS Photonics* **6**, 1485 (2019).
- [9] A. O. Govorov, Z. Fan, P. Hernandez, J. M. Slocik, and R. R. Naik, Theory of circular dichroism of nanomaterials comprising chiral molecules and nanocrystals: Plasmon enhancement, dipole interactions, and dielectric effects, *Nano Lett.* **10**, 1374 (2010).
- [10] N. A. Abdulrahman, Z. Fan, T. Tonooka, S. M. Kelly, N. Gadegaard, E. Hendry, A. O. Govorov, and M. Kadodwala, Induced chirality through electromagnetic coupling between chiral molecular layers and plasmonic nanostructures, *Nano Lett.* **12**, 977 (2012).
- [11] T. J. Davis and E. Hendry, Superchiral electromagnetic fields created by surface plasmons in nonchiral metallic nanostructures, *Phys. Rev. B* **87**, 085405 (2013).
- [12] B. M. Maoz, Y. Chaikin, A. B. Tesler, O. Bar Elli, Z. Fan, A. O. Govorov, and G. Markovich, Amplification of chiroptical activity of chiral biomolecules by surface plasmons, *Nano Lett.* **13**, 1203 (2013).
- [13] M. Schäferling, D. Dregely, M. Hentschel, and H. Giessen, Tailoring Enhanced Optical Chirality: Design Principles for Chiral Plasmonic Nanostructures, *Phys. Rev. X* **2**, 031010 (2012).

- [14] R. Tullius, A. S. Karimullah, M. Rodier, B. Fitzpatrick, N. Gadegaard, L. D. Barron, V. M. Rotello, G. Cooke, A. Laphorn, and M. Kadodwala, "Superchiral" spectroscopy: Detection of protein higher order hierarchical structure with chiral plasmonic nanostructures, *J. Am. Chem. Soc.* **137**, 8380 (2015).
- [15] R. Tullius, G. W. Platt, L. Khosravi Khorashad, N. Gadegaard, A. J. Laphorn, V. M. Rotello, G. Cooke, L. D. Barron, A. O. Govorov, A. S. Karimullah, and M. Kadodwala, Superchiral plasmonic phase sensitivity for fingerprinting of protein interface structure, *ACS Nano* **11**, 12049 (2017).
- [16] W. Zhang, T. Wu, R. Wang, and X. Zhang, Amplification of the molecular chiroptical effect by low-loss dielectric nanoantennas, *Nanoscale* **9**, 5701 (2017).
- [17] E. Mohammadi, K. L. Tsakmakidis, A. N. Askarpour, P. Dehkhoda, A. Tavakoli, and H. Altug, Nanophotonic platforms for enhanced chiral sensing, *ACS Photonics* **5**, 2669 (2018).
- [18] E. Mohammadi, A. Tavakoli, P. Dehkhoda, Y. Jahani, K. L. Tsakmakidis, A. Tittl, and H. Altug, Accessible superchiral near-fields driven by tailored electric and magnetic resonances in all-dielectric nanostructures, *ACS Photonics* **6**, 1939 (2019).
- [19] J. García-Guirado, M. Svedendahl, J. Puigdollers, and R. Quidant, Enhanced chiral sensing with dielectric nanoresonators, *Nano Lett.* **20**, 585 (2020).
- [20] Y. Luo, C. Chi, M. Jiang, R. Li, S. Zu, Y. Li, and Z. Fang, Plasmonic chiral nanostructures: Chiroptical effects and applications, *Adv. Opt. Mater.* **5**, 1700040 (2017).
- [21] S. Yoo and Q.-H. Park, Metamaterials and chiral sensing: A review of fundamentals and applications, *Nanophotonics* **8**, 249 (2019).
- [22] Y. Y. Lee, R. M. Kim, S. W. Im, M. Balamurugan, and K. T. Nam, Plasmonic metamaterials for chiral sensing applications, *Nanoscale* **12**, 58 (2020).
- [23] M. L. Solomon, A. A. E. Saleh, L. V. Poulikakos, J. M. Abendroth, L. F. Tadesse, and J. A. Dionne, Nanophotonic platforms for chiral sensing and separation, *Acc. Chem. Res.* **53**, 588 (2020).
- [24] X. Mu, L. Hu, Y. Cheng, Y. Fang, and M. Sun, Chiral surface plasmon-enhanced chiral spectroscopy: Principles and applications, *Nanoscale* **13**, 581 (2021).
- [25] Y. Zhao, A. N. Askarpour, L. Sun, J. Shi, X. Li, and A. Alù, Chirality detection of enantiomers using twisted optical metamaterials, *Nat. Commun.* **8**, 14180 (2017).
- [26] S. Droulias and L. Bougas, Absolute chiral sensing in dielectric metasurfaces using signal reversals, *Nano Lett.* **20**, 5960 (2020).
- [27] S. Droulias, Chiral sensing with achiral isotropic metasurfaces, *Phys. Rev. B* **102**, 075119 (2020).
- [28] M. L. Nesterov, X. Yin, M. Schäferling, H. Giessen, and T. Weiss, The role of plasmon-generated near fields for enhanced circular dichroism spectroscopy, *ACS Photonics* **3**, 578 (2016).
- [29] F. Graf, J. Feis, X. Garcia-Santiago, M. Wegener, C. Rockstuhl, and I. Fernandez-Corbaton, Achiral, helicity preserving, and resonant structures for enhanced sensing of chiral molecules, *ACS Photonics* **6**, 482 (2019).
- [30] M. L. Solomon, J. Hu, M. Lawrence, A. García-Etxarri, and J. A. Dionne, Enantiospecific optical enhancement of chiral sensing and separation with dielectric metasurfaces, *ACS Photonics* **6**, 43 (2019).
- [31] K. Yao and Y. Zheng, Near-ultraviolet dielectric metasurfaces: from surface-enhanced circular dichroism spectroscopy to polarization-preserving mirrors, *J. Phys. Chem. C* **123**, 11814 (2019).
- [32] J. Hu, M. Lawrence, and J. A. Dionne, High quality factor dielectric metasurfaces for ultraviolet circular dichroism spectroscopy, *ACS Photonics* **7**, 36 (2020).
- [33] S. Tretyakov and A. Viitanen, Waveguide and resonator perturbation techniques measuring chirality and nonreciprocity parameters of biisotropic materials, *IEEE Trans. Microwave Theory Tech.* **43**, 222 (1995).
- [34] M. Schäferling, X. Yin, and H. Giessen, Formation of chiral fields in a symmetric environment, *Opt. Express* **20**, 26326 (2012).
- [35] A. Yariv and P. Yeh, *Photonics: Optical Electronics in Modern Communications*, Oxford Series in Electrical and Computer Engineering (Oxford University Press, Oxford, 2007).
- [36] See Supplemental Material at <http://link.aps.org/supplemental/10.1103/PhysRevB.104.075412> for the theoretical formulation, the analytical derivation of signal reversals, the analytical derivation of formulas for the determination of unknown chirality with signal reversals, and further numerical examples.
- [37] P. B. Johnson and R. W. Christy, Optical constants of the noble metals, *Phys. Rev. B* **6**, 4370 (1972).
- [38] S. Droulias, A. Jain, T. Koschny, and C. M. Soukoulis, Novel Lasers Based on Resonant Dark States, *Phys. Rev. Lett.* **118**, 073901 (2017).
- [39] S. Droulias, A. Jain, T. Koschny, and C. M. Soukoulis, Fundamentals of metasurface lasers based on resonant dark states, *Phys. Rev. B* **96**, 155143 (2017).
- [40] S. Droulias, T. Koschny, and C. M. Soukoulis, Finite-size effects in metasurface lasers based on resonant dark states, *ACS Photonics* **5**, 3788 (2018).
- [41] D. Sofikitis, L. Bougas, G. E. Katsoprinakis, A. K. Spiliotis, B. Loppinet, and T. P. Rakitzis, Evanescent-wave and ambient chiral sensing by signal-reversing cavity ringdown polarimetry, *Nature (London)* **514**, 76 (2014).
- [42] L. Bougas, D. Sofikitis, G. E. Katsoprinakis, A. K. Spiliotis, P. Tzallas, B. Loppinet, and T. P. Rakitzis, Chiral cavity ring down polarimetry: Chirality and magnetometry measurements using signal reversals, *J. Chem. Phys.* **143**, 104202 (2015).
- [43] C. Kelly, L. Khosravi Khorashad, N. Gadegaard, L. D. Barron, A. O. Govorov, A. S. Karimullah, and M. Kadodwala, Controlling metamaterial transparency with superchiral fields, *ACS Photonics* **5**, 535 (2018).
- [44] <https://www.comsol.com>.
- [45] R. Zhao, J. Zhou, T. Koschny, E. N. Economou, and C. M. Soukoulis, Repulsive Casimir Force in Chiral Metamaterials, *Phys. Rev. Lett.* **103**, 103602 (2009).
- [46] J. C. Visschers, O. Tretyakov, D. Budker, and L. Bougas, Continuous-wave cavity ring-down polarimetry, *J. Chem. Phys.* **152**, 164202 (2020).
- [47] A. Tittl, A. Leitis, M. Liu, F. Yesilkoy, D.-Y. Choi, D. N. Neshev, Y. S. Kivshar, and H. Altug, Imaging-based molecular barcoding with pixelated dielectric metasurfaces, *Science* **360**, 1105 (2018).